NJC

PAPER

View Article Online
View Journal | View Issue

Cite this: *New J. Chem.*, 2023, **47**, 2626

Received 4th November 2022,
Accepted 27th December 2022

DOI: 10.1039/d2nj05433g

rsc.li/njc

Superparamagnetic cobalt ferrite nanoparticles synthesized by gamma irradiation†

Amel Zorai,[ab] Abdelhafid Souici,*[a] Diana Dragoe,[c] Eric Rivière,[c] Salim Ouhenia,[a] Jacqueline Belloni[b] and Mehran Mostafavi*[b]

The radiolytic method is used to synthesize ultrasmall cobalt ferrite nanoparticles, $CoFe_2O_4$, exhibiting superparamagnetic properties. These systems are investigated by studying their properties at increasing dose of the irradiation process. These magnetic nanoparticles (MNPs) are characterized by X-ray diffraction (XRD), high-resolution transmission electronic microscopy (HRTEM), energy dispersive spectroscopy (EDS), and X-ray photoelectron spectroscopy (XPS). The XRD analysis and HRTEM observations confirm the formation of ultra-small cobalt ferrite nanoparticles (NPs) of $CoFe_2O_4$ (6–9 nm) in the cubic spinel structure. The temperature-dependent magnetic measurements reveal that the NPs exhibit superparamagnetic properties with a high magnetization $M_s \sim 70$ Am^2 kg^{-1} at 300 K and a very low coercivity (0.9 mT).

Introduction

Magnetic nanoparticles (MNPs) exhibit interesting physical and chemical properties for a wide range of technological applications, principally in catalysis,[1] magnetic storage technology,[2,3] spintronic devices,[4] and biomedicine.[5,6] When the magnetic behaviour is observed at temperature higher than the blocking temperature (T_B), the material is superparamagnetic.[7]

Superparamagnetic cobalt ferrite NPs $CoFe_2O_4$ (or mixed iron and cobalt oxides) exhibit excellent properties of high saturation magnetization (M_s) and magnetocrystalline anisotropy, low coercivity (H_C) and remanent magnetization (M_r), and high chemical stability and mechanical hardness.[8] They have thus been used in nanomedicine in both diagnostic and therapeutic applications such as magnetic resonance imaging (MRI),[9] drug delivery,[10] and especially magnetic hyperthermia therapy (MHT) for cancer treatment.[11–13]

The synthesis of cobalt ferrite $CoFe_2O_4$ has been extensively explored by various methods including co-precipitation,[14,15] sol–gel,[16] solvothermal,[17] hydrothermal,[18] thermal decomposition,[19,20] reduction in boiling polyol,[21] or alkalide in ethers (Table S1, ESI†).[22]

Over the past 40 years, radiation-induced synthesis has been extensively used to prepare metal and semiconductor nanoscale particles,[23–25] including metal sulfides.[26,27] This method at ambient temperature and pressure, avoiding the use of reducing chemical agents that could contaminate the product and lead to side reactions, offers a powerful alternative way for the synthesis of nanoparticles with high dispersity. This method allows controlling particle nucleation and the final size of the particles. The room temperature conditions aid in preventing sintering. In addition, the pulse radiolysis technique offers the possibility of studying in real time the different growth steps of the metal.[28,29]

Recently, the radiolytic route has been used for the synthesis of monodisperse small and MNPs of iron oxide Fe_3O_4,[30–32] manganese oxide Mn_3O_4,[33,34] cobalt oxide Co_3O_4,[35] and cobalt hydroxide α-$Co(OH)_2$.[36] However, mixed cobalt and iron oxide $CoFe_2O_4$ (or cobalt ferrite) has not yet been synthesized by the radiolytic method.

The aim of the current study is to give particular attention to the γ-induced reduction of cobaltic hydroxide in a mixed solution with ferric iron hydroxide and the mechanism of synthesis of ultra-small cobalt ferrite nanoparticles in the presence of polyvinylpyrrolidone (PVP) as a biocompatible stabilizer molecule,[37] and to investigate their magnetic properties. In fact, our work aims to obtain efficient MNPs for MHT for cancer treatment which is a potential application. Therefore, we report here the influence of the dose and the size of MNPs on their magnetic properties.

Experimental section

Materials

All chemical reagents were of high grade and purity and were purchased from Sigma-Aldrich.

---

[a] *Laboratoire de Physico-Chimie des Matériaux et Catalyse, Faculté des Sciences Exactes, Université de Bejaia, Bejaia 06000, Algeria*

[b] *Institut de Chimie Physique, UMR 8000, CNRS, Université Paris-Saclay, Bâtiment 349, Campus d'Orsay, 15 Avenue Jean Perrin, 91405, Orsay Cedex, France*

[c] *Institut de Chimie Moléculaire et des Matériaux d'Orsay, UMR 8182, CNRS, Université Paris-Saclay, Bâtiment Henri Moissan, 19 avenue des Sciences, 91400, Orsay, France*

† Electronic supplementary information (ESI) available. See DOI: **https://doi.org/10.1039/d2nj05433g**

General procedure for radiation-induced synthesis

Analogous to the radiolytic synthesis of iron oxide Fe_3O_4,[27–31] this method was also used to prepare cobalt ferrite nanoparticles. Because of their high energy, the radiation penetrates throughout the precursor solution, and, under selective conditions, generates from water, at room temperature and without any added chemical agent, strongly reducing species that are homogeneously distributed. At an adequate dose, one-third of the trivalent cations are thus reduced into divalent ions with the same distribution. Compared to chemical reduction at high temperature, the final nanoparticles are free of any chemical agent and smaller because they do not undergo sintering. The one pot radiolytic method has been successfully used for reduction into metal nanoparticles,[23] and more recently, for the reduction of trivalent hydroxides into Me_3O_4.[27–31]

Cobalt ferrite is a mixed oxide of trivalent iron and divalent cobalt ions. To synthesize these ions in an intimate mixture, our approach is to oxidize first, under aerated basic conditions (NH_4OH), the cobalt ions from Co^{II} to Co^{III} in a solution containing Co^{II} and Fe^{III}. An ammoniated complex of trivalent cobalt ions is formed before being precipitated together with trivalent iron ions. Then, the penetrating γ-radiation in solution reduces the Co^{III} ions back into Co^{II} homogeneously inside the mixed hydroxide particles at room temperature.

For this purpose, the solutions were prepared by mixing chloride hexahydrate iron(III) ($FeCl_3$, $6H_2O$ at 4×10^{-3} mol L^{-1}), and cobalt(II) chloride hexahydrate ($CoCl_2$, $6H_2O$, at 2×10^{-3} mol L^{-1}). Therefore, the stoichiometry of the metal atoms in the precursor solution is Fe/Co = 2 as required by the synthesis of cobalt ferrite. The solution was mixed with 2-propanol ($(CH_3)_2CHOH$) at 0.13 mol L^{-1} in order to scavenge the radiolytic oxidizing radicals $OH^{\bullet}$ (much more efficiently than the diluted Cl^- ions), and with polyvinylpyrrolidone (PVP) M.W. ∼ 10 000, as the particle stabilizer. PVP is attractive for medical applications because it is biodegradble, non-poisonous, pH-stable and heat-resistant.[38] The PVP concentration was 10^{-3} mol L^{-1} only in order to avoid any cross-linking by radical scavenging. The solution pH was finally adjusted to 11.8 by adding ammonium hydroxide (NH_4OH) to produce a colloidal suspension of trivalent iron and cobalt hydroxides intimately mixed. Without the cobalt salt, the Fe^{III} solution is readily replaced by a light rust-orange colloidal suspension, whereas, without the iron salt, the pink Co^{II} solution would be oxidized to a clear brown solution of Co^{III} hydroxide. When NH_4OH is added to the mixed solution of both ions, the colloid becomes orange-brown and the supernatant solution becomes colorless, indicating the formation of colloidal particles of cobalt and ferric hydroxides.

$$2FeCl_3 + CoCl_3 + 9OH^- \rightarrow (Fe^{III}(OH)_3)_2,\ Co^{III}(OH)_3 + 9Cl^- \tag{1}$$

Before irradiation, the samples were thoroughly deaerated in small flasks (10 ml) for approximately 10 min by flushing with nitrogen to remove the O_2. The samples were then exposed to a panoramic γ-^{60}Co source at a dose rate of ≈2.3 kGy h^{-1}.

During the colloidal solution irradiation, the major part of the energy is absorbed by the most abundant water molecules (reaction (1)):

$$H_2O \xrightarrow{\gamma\,\text{irradiation}} e_{aq}{}^-(2.8), H^+(2.8),\ H^{\bullet}(0.62),\ H_2(0.47),\ H^{\bullet}(2.8),\ H_2O_2(0.73) \tag{2}$$

(The radiolytic yields of the products of water radiolysis in 10^{-7} mol J^{-1} unit are in brackets).[39]

Under basic conditions (pK = 9.6), the $H^{\bullet}$ radicals are scavenged by the anions OH^- and are replaced by e^-_{aq}:

$$H^{\bullet} + OH^- \rightarrow e^-_{aq} \tag{3}$$

The radicals $OH^{\bullet}$ are scavenged by isopropanol, and the strongly reducing radicals $(CH_3)_2C^{\bullet}OH$ are formed (reactions (3)):

$$OH^{\bullet} + (CH_3)_2CHOH \rightarrow (CH_3)_2C^{\bullet}OH + H_2O \tag{4}$$

Therefore, under these conditions of irradiation with the formation of e^-_{aq} and $(CH_3)_2C^{\bullet}OH$ radicals, the medium under irradiation is strongly reductive.

Characterization of cobalt ferrite nanoparticles

The UV-visible spectra of the solutions were recorded before and after irradiation using a Hewlett-Packard 8453A UV-visible spectrophotometer.

The crystalline structures were evaluated by grazing incidence (3°) X-ray diffraction performed on a Panalytical X'pert pro MRD diffractometer with Cu Kα radiation (λ = 0.15418 nm). The patterns were obtained by step scanning from 15° to 90° in 2θ with an increment of 0.0752° and a counting time of 1800 s per step. Crystallographic phases were identified according to JCPDS files No. 22-1086 and fitted by MAUD Rietveld refinement software.[40] The LaB_6-SRM660a standard was used to calibrate the instrument broadening. An isotropic model was used to refine the mean nanoparticle size. During Rietveld refinement, the microstrains and cell parameters were refined to obtain the best reliability factors.

The magnetic measurements of the $CoFe_2O_4$ nanoparticles were performed using a Superconducting Quantum Interference Device (SQUID) magnetometer (MPMS XL7 Quantum Design). Zero-field cooling (ZFC) and field cooling (FC) magnetization curves were measured at different temperatures with a constant temperature sweep rate of 2 K min^{-1} and a magnetic field of 5 mT. Isothermal magnetization studies were also performed at temperatures of 5 and 300 K by measuring the hysteresis curves in the range of $-5\ T \leq H \leq 5\ T$. The samples were blocked with glue to avoid orientation with respect to the magnetic field.

The cobalt ferrite nanoparticle morphology, size distribution and stoichiometry were investigated by high-resolution transmission electron microscopy (HRTEM), selected area electron diffraction (SAED), and energy dispersive spectroscopy (EDS) using a JEOL 2100 Plus instrument working at 200 kV fitted with a GATAN Rio 16 camera and an IDFix EDS system from SAMx.

X-ray photoelectron spectroscopy (XPS) measurements were performed using a Thermo Fisher Scientific instrument with a monochromatic Al-Kα X-ray source (energy 1486.7 eV). The samples were measured as compacted powders and fixed using an aluminium foil mask. The base pressure was approximately 5×10^{-9} mbar and the diameter of the X-ray beam spot was 200 μm, corresponding to an irradiated surface of approximately 0.5 mm^2. The hemispherical analyzer was operated at a 0° take-off angle in Constant Analyzer Energy (CAE) mode. Wide-scan spectra were recorded at a pass energy of 200 eV and an energy step of 1 eV, while narrow-scan spectra were recorded at pass energies of 50 eV and 20 eV with an energy step of 0.1 eV. Charge compensation was achieved with the help of a "dual beam" flood gun using low-energy electrons (<5 eV) and argon ions. The binding energy scale was calibrated on neutral carbon set at 285 eV, which corresponds to a value of 529.9 eV for the oxide component in the O 1s core-level spectrum.

Results and discussion

Synthesis of cobalt ferrite nanoparticles

Under reducing conditions, the cobaltic ions, preferentially over the ferric ions, are reduced by both hydrated electrons and isopropyl radicals:

$$e^-_{aq} + Co^{III}(OH)_3, (Fe^{III}(OH)_3)_2 \rightarrow Co^{II}(OH)_2, 2Fe^{III}(OH)_3, + OH^- \tag{5}$$

$$(CH_3)_2C^{\bullet}OH + Co^{III}(OH)_3, (Fe^{III}(OH)_3)_2 \rightarrow Co^{II}(OH)_2, (Fe^{III}(OH)_3)_2 + (CH_3)_2CO + H_2O \tag{6}$$

The ferric ions may also be reduced as well:

$$e^-_{aq} + Co^{III}(OH)_3, (Fe^{III}(OH)_3)_2 \rightarrow Co^{III}(OH)_2, Fe^{II}(OH)_2, Fe^{III}(OH)_3 + OH^- \tag{7}$$

$$(CH_3)_2C^{\bullet}OH + Co^{III}(OH)_3, (Fe^{III}(OH)_3)_2 \rightarrow Co^{II}(OH)_2, Fe^{II}(OH)_2, Fe^{III}(OH)_3, (CH_3)_2CO + H_2O \tag{8}$$

However, the valency II of cobalt ions is more stable than that of iron ions, and internal electron transfer occurs from Fe^{II} to Co^{III}. Therefore, cobalt ions are preferentially reduced:

$$Co^{III}(OH)_3, Fe^{II}(OH)_2, Fe^{III}(OH)_3 \rightarrow Co^{II}(OH)_2, (Fe^{III}(OH)_3)_2 \tag{9}$$

The cobalt-ferric hydroxide progressively loses water molecules and precipitates into black nanoparticles of the cobalt ferrite $CoFe_2O4$, stabilized by their interactions with PVP:

$$Co^{II}(OH)_2, (Fe^{III}(OH)_3)_2 \rightarrow \cdots \rightarrow Co^{II}(OH)_2, 2FeO(OH)_2 + H_2 \rightarrow CoFe_2O_4 + 4H_2O \tag{10}$$

It is like that hydroxide anions OH$^-$ are still adsorbed on the nanoparticle surface.

First, it is worth noting that the cobalt ferrite nanoparticles are very stable with respect to oxidation, especially when the flasks are open to air, in contrast to the Fe_3O_4 nanoparticles which were partially reoxidized.[41] Then, the characterization measurements were found to be constant during aging.

Optical properties

The basic solution of Fe^{III} and Co^{III} is initially orange-brown and turns progressively pale gray at increasing doses. After approximately 8 kGy, small black particles were immediately attracted by a magnet across the glass wall of the flask (Fig. 1). Thus, these particles display magnetic properties. Without agitation or magnetic attraction, the particles precipitate slowly.

The formation and growth of nanoparticles were followed by UV-visible measurements up to irradiation doses of 60 kGy. Before irradiation, the solution presented a broad absorbance band between 300 and 500 nm, which was assigned to mixed Fe^{III} and Co^{III} hydroxide formed by adding ammonia to the iron(III) chloride and cobalt(II) chloride solutions.

The intensity of the absorbance band at 306 nm, which is assigned to the Fe^{III} complex, first decreases to a minimum at 8 kGy, whereas the broad band above 400 nm increases with an isosbestic point at ≈ 390 nm (Fig. S1, ESI†). The minimum is assigned to the complete formation of cobalt ferrite particles absorbing widely up to 800 nm. In the second step, after 8 kGy, the absorbance increases at any wavelength because of the increasing light scattering of growing agglomerates between the magnetic particles into larger agglomerates.

The radiolytic yield corresponding to the complete reduction of Co^{III} ions at 8 kGy is equal to $G(Co^{II}) = 2 \times 10^{-3}$ mol L^{-1}/8×10^3 Gy = 2.5×10^{-7} mol J^{-1}. This value is less than the total reducing yield (6.2×10^{-7} mol J^{-1}) (eqn (2) because the concentration of hydroxide colloidal particles is much lower than that of Co^{III}, and the radical scavenging competes with radical recombination.

Crystallographic structure

Fig. 2 presents the XRD patterns of the nanoparticles synthesized at doses of 6, 8, 16, and 60 kGy.

The XRD patterns demonstrate that the diffraction peaks situated at the positions 18.32°, 30.13°, 35.49°, 43.14°, 57.05°, and 62.65° correspond to the (111), (220), (311), (400), (511), and (440) planes, respectively. At the three doses ≥ 8 kGy, these results correspond to the spinel structure of the $CoFe_2O_4$ compound with space group $Fd\bar{3}m$ (No 227) and a lattice

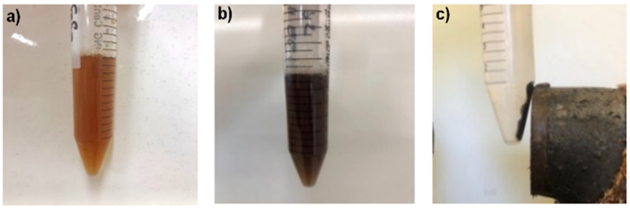

Fig. 1 Solution before and after irradiation. (a) Colloidal solution of mixed Co and Fe hydroxides before irradiation (0 kGy). (b) Solution after 8 kGy and shaking. (c) Black nanoparticles of (b) attracted by a magnet and transparent colorless supernatant.

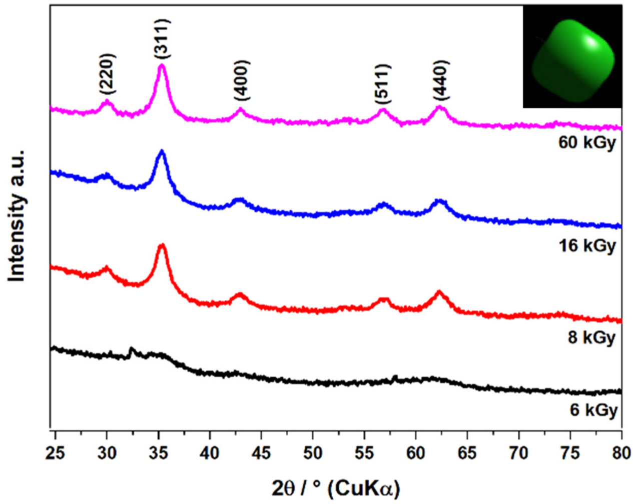

Fig. 2 X-Ray diffraction patterns of nanoparticles formed after irradiation doses of 6, 8, 16 and 60 kGy of a solution containing 4×10^{-3} mol L^{-1} iron(III) chloride hexahydrate ($FeCl_3$, $6H_2O$), 2×10^{-3} mol L^{-1} cobalt(II) chloride hexahydrate ($CoCl_2$, $6H_2O$) 10^{-3} mol L^{-1} PVP, and 0.13 mol L^{-1} isopropanol. Inset: the shape of the crystallite at 60 kGy obtained by the Rietveld simulation.

parameter a = 8.43 Å, very close to that of JCPDS card No. 22-1086 with a lattice parameter a = 8.392 Å.

The anisotropic nanoparticle diameter obtained by the Rietveld refinement is 6–8 nm (Table 1). It is observed that the nanoparticle size increases slightly with an increasing dose. Moreover, the XRD patterns are similar at all the doses except 6 kGy, indicating that the reduction is completed only for doses ≥ 8 kGy (Fig. 2).

This dose also corresponds to the minimum observed in the optical absorption spectrum (Fig. S1, ESI†). Actually, the concentration of the colloidal particles $Co^{III}(OH)_3$, $(Fe^{III}(OH)_3)_2$ is several times lower than the precursor Co^{III} concentration and their radical scavenging undergoes a significant competition with the radical recombination. Another remarkable feature is that the XRD spectrum of the spinel structure is identical in the range of 8–60 kGy (Fig. 2). The further reduction in the nanoparticles is thus negligible, because in the flask bottom, they are much less subjected to the attack of the radicals formed in the bulk. In addition, geminate ion recombination in these crystallites after their direct irradiation hinders further reduction.

Table 1 Structural characteristics of radiation-induced cobalt ferrite nanoparticles

Dose (kGy)	D (nm) (XRD)	D (nm) (HRTEM)	a (Å) (XRD)[a]	Fe/Co (EDS)	Fe^{3+}/Co^{2+} (XPS)
6	—	—	—	—	1.9
8	6.7 (0.2)	7.3 (1.5)	8.43 (0.01)	2.1	1.4
16	7.0 (0.1)	—	8.43 (0.03)	1.9	0.9
20	7.9 (0.3)	9.6 (1.0)[b]	8.40 (0.02)	1.8	1.1
60	8.4 (0.1)	10.1 (1.5)[b]	8.43 (0.01)	2.0	1.0

[a] Lattice parameter of the spinel structure in JCPDS card No. 22-1086: a = 8.392 Å. [b] See size distribution (fig. S2, ESI).

Microscopy imaging of radiation-induced cobalt ferrite nanoparticles

The morphological properties and size distribution of the synthetized nanoparticles were investigated using transmission electron microscopy (TEM) and high-resolution transmission electron microscopy (HRTEM). The images in Fig. 3 illustrate the morphology of the nanoparticles formed at 8 kGy. The $CoFe_2O_4$ nanosized particles stabilized by the PVP agent are monodisperse with a spherical- shape. However, it appears on the images that a few of them are isolated, very small, and at the limit of the TEM observation, while the majority of the nanoparticles are agglomerated, probably because of the powerful dipole–dipole interactions between the magnetic nanoparticles, which may facilitate their agglomeration. The corresponding SAED diagram (Fig. 3b) confirms the spinel structure observed by XRD. In the HRTEM images, the distances between the planes are d(311) = 2.5 Å (Fig. 3c) and d(211) = 4.8 Å (Fig. 3d). The lognormal distribution fit of the nanoparticles is 6–8 nm for an

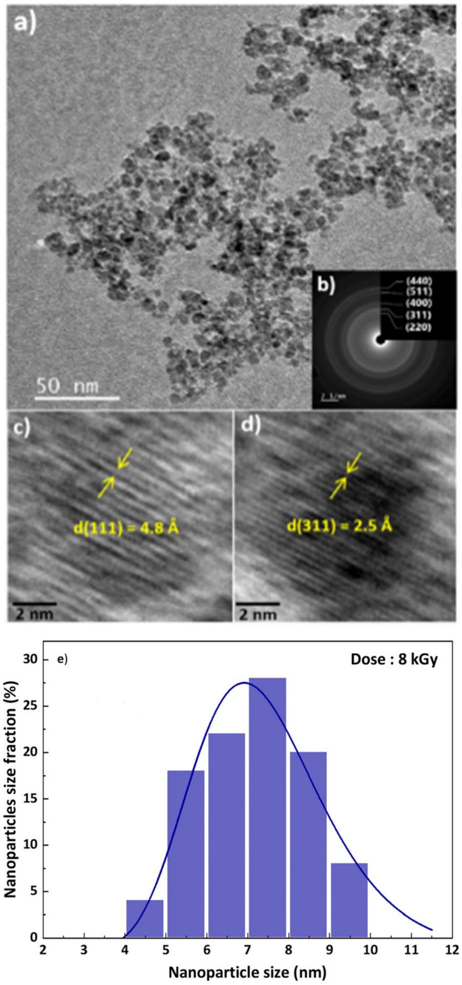

Fig. 3 Microscopy images of radiation-induced cobalt ferrite nanoparticles formed at 8 kGy. (a) TEM image. (b) SAED micrograph. (c) and (d) HRTEM images of interplanar distances. (e) Histogram of the size distribution and lognormal fit, D = 7.3 ± 1.5 nm.

irradiation dose of 8 kGy (Fig. 3e), which is in agreement with the XRD observations.

The stoichiometry of the cobalt ferrite nanoparticles analysed using EDS is shown in Table 1. The ratio of Fe and Co ions is close to Fe/Co = 2. These results clearly demonstrate the radiolytic formation in ammonia solutions and in the presence of PVP of the ultra-small cobalt ferrite $CoFe_2O_4$ nanoparticles.

Notably, the Fe/Co ratio is the same at 8 kGy, where the reduction is complete, according to the dose-dependence of the absorption spectrum (Fig. S1, ESI†), and at higher doses. It seems that the precipitation of particles of $CoFe_2O_4$ to the flask bottom protects them from a further reduction by the radicals. Even then, they are still directly irradiated, and the recombination of charges in the small solid crystals avoids the reduction.

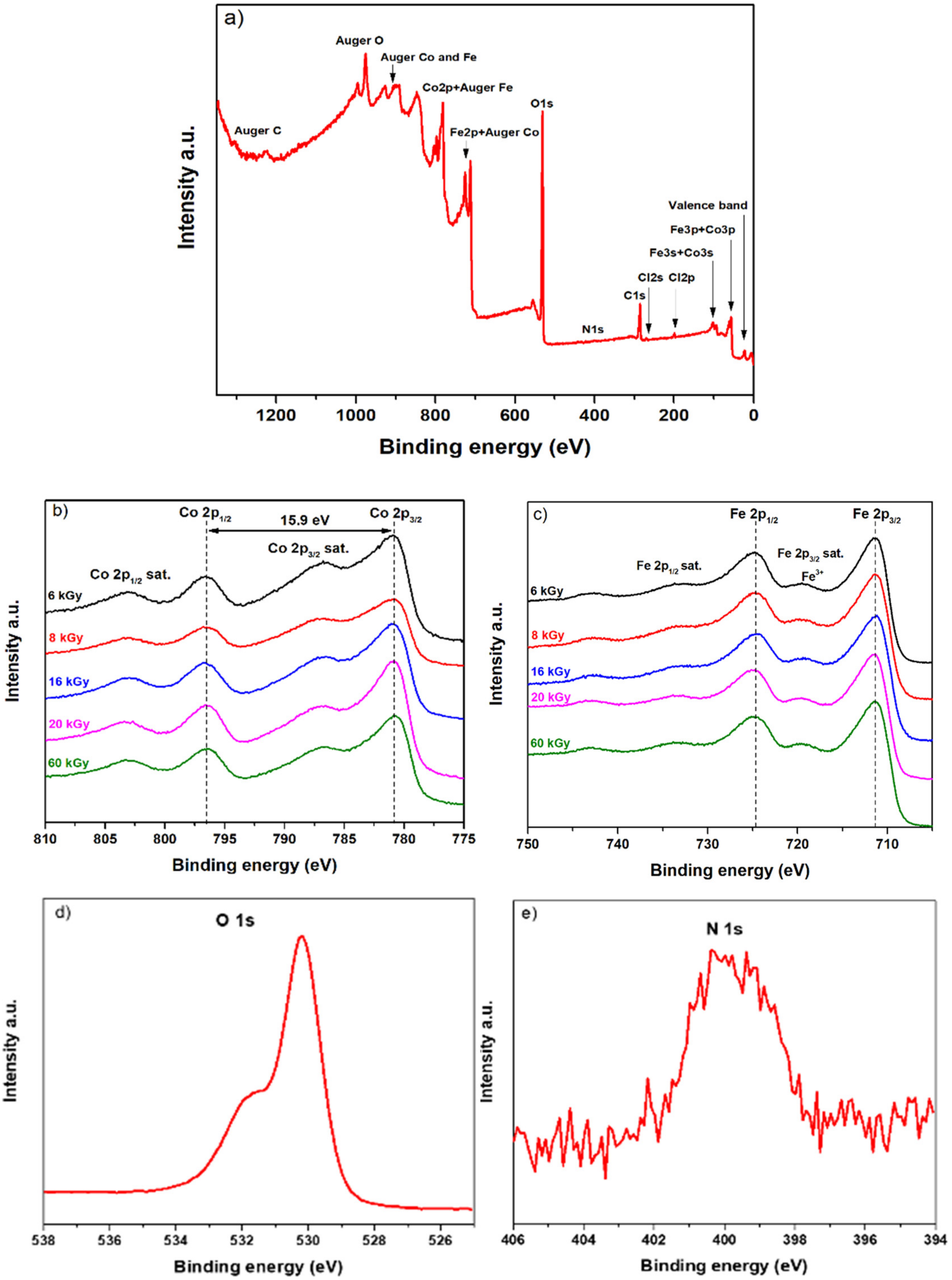

Fig. 4 XPS spectra of radiation-induced cobalt ferrite nanoparticles. (a) XPS survey. (b) Co 2p. (c) Fe 2p. (d) O 1s. (e) N 1s.

X-ray photoelectron spectroscopy analysis

XPS measurements were conducted to reveal the surface information of radiation-induced cobalt ferrite nanoparticles. The XPS survey spectrum (Fig. 4a) shows peaks corresponding to the Co 2p, Fe 2p, O 1s, C 1s, N 1s, and Auger signals. The Co 2p core-level spectrum (Fig. 4b) is composed of two main peaks located at 780.4 eV and 796.1 eV corresponding to Co $2p_{3/2}$ and Co $2p_{1/2}$. The presence of a satellite peak at $\sim$6 eV from the main Co $2p_{3/2}$ peak and its intensity suggest that Co is present on the surface mainly as Co^{2+}, as also indicated by the spin-orbit splitting which is 15.8 eV.[42,43] The Fe 2p core-level spectra shown in Fig. 4c show the spin–orbit doublet Fe $2p_{3/2}$ and Fe $2p_{1/2}$ located at 711 eV and 724.5 eV, respectively, with the shake-up satellite peak at 719.3 eV present in all spectra, confirming the valence state 3^+.[44–48] These spectra confirm the presence of Co^{2+} and Fe^{3+} ions located at octahedral and tetrahedral sites in the $CoFe_2O_4$ lattice.[49] There is reciprocal interference between the Co et Fe 2p lines and Auger signals. An attempt was made to subtract the Auger signals, as in ref. 49 and the results are shown in Fig. S3 (ESI†). No further attempt to decompose the Fe 2p and Co 2p difference spectra was made as this subtraction represents an additional source of error. The O 1s core-level spectrum in Fig. 4d may be decomposed into two main contributions, one located at approximately 529.9 eV corresponding to the lattice oxygen in the Co/Fe-oxygen framework, and the second at 531.7 eV attributed to the oxygen originating from the surface hydroxide and to oxygen in polyvinylpyrrolidone.

The N1s core-level spectrum (Fig. 4e) centered at 400 eV confirms the presence of the PVP coating on the cobalt ferrite particle surface. The Fe/Co surface ratio at the particles surface, as measured by XPS with increasing dose from 6 to 16 kGy, is reported in Table 1. Remarkably, it decreases, whereas it is confirmed by EDS that the ions contained in the particles have the same ratio of 2 as the salt precursors. It seems that, slowly under irradiation, an exchange occurs between the inner Co^{2+} and the outer Fe^{3+}.[50]

Magnetic properties of radiation-induced cobalt ferrite nanoparticles

The magnetic properties of small cobalt ferrite nanoparticles were studied using a SQUID under a low external magnetic field (H = 5 mT) as a function of temperature.

Fig. 5 presents the zero-field-cooled (ZFC) and field cooled (FC) temperature-dependent magnetization curves between 10 and 400 K for 8 and 60 kGy. The maximum of the ZFC curve corresponds to the blocking temperature (T_B). T_{irr} corresponds to the irreversibility temperature at which the ZFC and FC curves merge and where the magnetic moments are unblocked. Above this temperature, superparamagnetic behavior is observed.[51] Below $T \approx 200$ K, the FC curves show saturated magnetization with temperature-independent behavior, which confirms the presence of the dipolar and interparticle coupling interaction effects.[52] As illustrated in Fig. 5, it is clear from the ZFC and FC curves that the blocking temperatures T_B for 8 and 60 kGy are 273 and 315 K, respectively. The increasing of the blocking temperature with the increasing dose is due to the increasing magnetocrystalline anisotropy associated with the spin-orbital coupling effect of Co^{2+}.[53] For both doses, the difference between T_{irr} and T_B suggests the presence of particle interactions due to surface spin disorder.[54] The hysteresis loop curves of radiation-induced cobalt ferrite nanoparticles, $CoFe_2O_4$, formed after 8, 20, and 60 kGy were recorded at 5, 100, and 300 K (Fig. 6 and Fig. S4, ESI†).

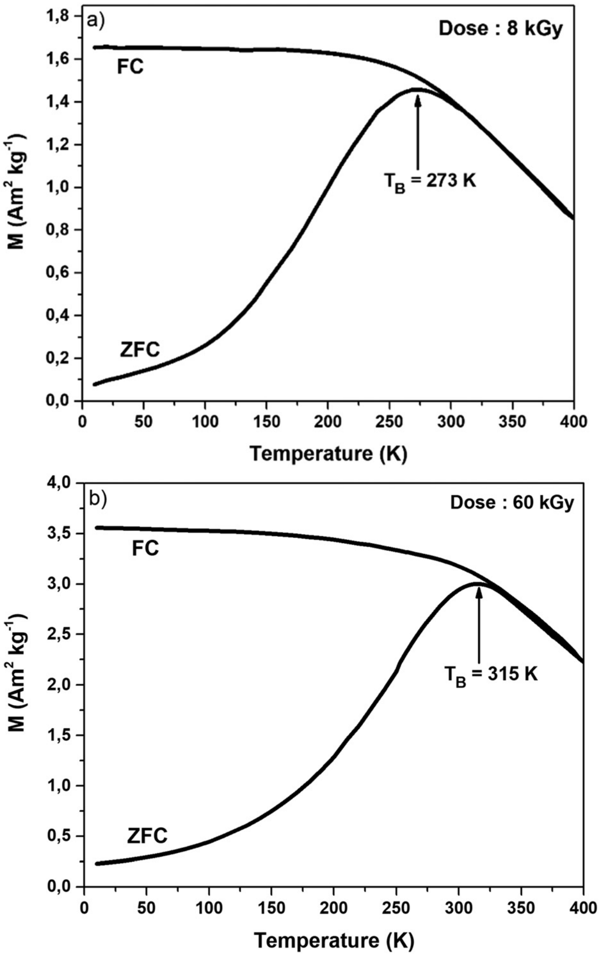

Fig. 5 DC magnetization curves obtained for $CoFe_2O_4$, formed at 8 and 60 kGy, respectively, under zero-field-cooled (ZFC) and field cooled (FC) conditions. Magnetic field H = 50 Oe.

The magnetic parameters, T_B, T_{irr}, remanence magnetization (M_r), coercive field (Hc), saturation magnetization (M_S), magnetic anisotropy (K), and the squareness ratio $R = M_r/M_S$, are summarized in Table 2.

At a very low temperature of 5 K (Fig. 6), the radiation-induced $CoFe_2O_4$ NPs exhibit ferrimagnetic behavior with a large coercivity. According to the Stoner-Wohlfarth model, the H_C values depend not only on the nanoparticle size and shape, but also on the surface spin and interparticle interaction.[55,56] By increasing the dose up to 60 kGy, the H_C value decreases.[57] It has been reported that gamma radiation softens the materials by reducing coercivity. Remarkably, the saturation magnetization

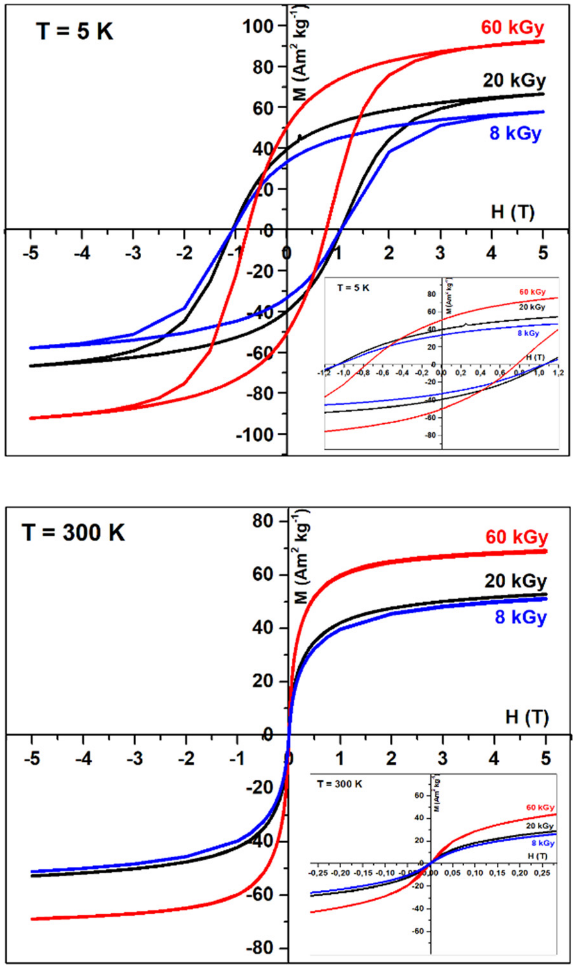

Fig. 6 Hysteresis loops of the magnetization (*M*) *versus* the magnetic field (*H*), measured at T = 5 K (top) and 300 K (down) of radiation-induced cobalt ferrite nanoparticles formed at the doses 8, 20 and 60 kGy. Insets: Magnification of the low field region.

value of $CoFe_2O_4$ NPs at 5 K, M_S = 92.5 Am^2 kg^{-1} at 60 kGy, is as high as for the bulk (M_s = 93 Am^2 kg^{-1}).

The ratio R is 0.54–0.59 for the nanoparticles formed at 8–60 kGy, respectively. The corresponding values of R are slightly larger than those obtained for noninteracting single-domain NPs with uniaxial anisotropy (R = 0.50) and less than those of NPs with cubic magnetocrystalline anisotropy (R = 0.83). Even though cobalt ferrite in the bulk has cubic anisotropy, the existence of an effective uniaxial anisotropy in magnetic nanoparticles has been attributed to surface effects at smaller crystallite sizes.[22]

Therefore, in a first approximation, assuming a noninteracting system of nanoparticles with uniaxial anisotropy, the magnetic anisotropy constant K may be estimated as a function of size at T_B using the equation $K = 25k_BT_B/V_m$ where k_B is the Boltzmann constant and V_m is the median volume.[22,58] The corresponding anisotropy constant values of 5.98 × 10^5 J m^{-3} for nanoparticles formed at 8 kGy is significantly higher than that of $CoFe_2O_4$ bulk materials (3.0 × 10^5 J m^{-3}). However, by increasing the dose, the magnetic anisotropy decreases and approaches the bulk value. The same phenomenon was reported for $CoFe_2O_4$ NPs synthesized using the sol-gel auto-combustion method and then irradiated at 50 and 100 kGy.[59] It is explained that γ-irradiation modifies the surface and the interparticle contact, which has a direct relationship with dipolar and exchange mechanisms, and therefore magnetic anisotropy.

The observed negligible coercivity H_C and remanence magnetization M_r at 300 K indicate that the $CoFe_2O_4$ NPs are superparamagnetic. Superparamagnetism is an essential feature for biomedical applications of these nanoparticles. The significant decrease of the ratio values up to 0.005 confirms a change in the magnetocrystalline anisotropy from cubic to uniaxial in a single magnetic domain.[60] The coercivity value at 60 kGy is less than that at 8 and 20 kGy, because the monodomain responsible for the superparamagnetism is larger.

The saturation magnetization increases with dose from 50.9 Am^2 kg^{-1} at 8 kGy to 69.2 Am^2 kg^{-1} at 60 kGy (Table 2), in parallel with the slight increase of the nanoparticle size (Table 1). Gamma irradiation as a post-treatment to synthesis has been indeed reported to play an important role in the redistribution of cations in ferrite structures,[16] and thus, to increase the magnetization values with the dose.

The M_s values for $CoFe_2O_4$ nanoparticles at 300 K (69.2 Am^2 kg^{-1}) are close to those of the $CoFe_2O_4$ bulk synthesized by the organic phase process (80 Am^2 kg^{-1}).[53] It is suggested that the magnetic moment disorder at the particle surface is responsible for the magnetization lowering with respect to the bulk.[53] Moreover, by the radiation-induced method in water without any heat treatment, the M_s values are among the highest values found for nanoparticles of cobalt ferrite of a similar size prepared by other methods, but after heating and/or annealing (Table S1, ESI†) such as coprecipitation,[61,62] hydrothermal,[18] thermal decomposition,[20,63] and polyol method[21] (Table S1, ESI†). Moreover, in radiation-induced synthesis, any possible adsorption of toxic additives is avoided in view of medical applications.

Table 2 Magnetic parameters of radiation-induced cobalt ferrite nanoparticles obtained from the fit of hysteresis loops for 8, 20 and 60 kGy at 5 and 300 K

Dose (kGy)	T_B (K)	T_{irr} (K)	K (10^5 J m^{-3})	$H_C^{5\ K}$ (T)	$M_r^{5\ K}$ (Am^2 kg^{-1})	$M_s^{5\ K}$ (Am^2 kg^{-1})	$R^{5\ K}$	$H_C^{300\ K}$ (10^{-4} T)	$M_r^{300\ K}$ (Am^2 kg^{-1})	$M_s^{300\ K}$ (Am^2 kg^{-1})	$R^{300\ K}$
8	273	310	5.98	1.06	33.3	57.9	0.57	17.8	0.47	50.9	0.009
20	—	—	—	1.02	39.5	66.7	0.59	16.3	0.46	52.8	0.009
60	315	395	3.55	0.76	50.3	92.5	0.54	9.1	0.38	69.2	0.005

Conclusion

Using the gamma-radiolysis technique, we successfully synthesized for the first time ultra-small magnetic $CoFe_2O_4$ nanoparticles with sizes less than 10 nm. Cobalt(III) cations were reduced, without heat or chemical agents, in the presence of iron(III) cations and PVP as a biocompatible stabilizer polymer. The nanoparticles were highly stable during aging. The XRD analysis confirmed the spinel structure of the $CoFe_2O_4$ nanoparticles obtained at doses between 8 and 60 kGy. An Fe/Co ratio of 2 was measured using EDS. SQUID magnetic measurements revealed that the nanoparticles have superparamagnetic properties above 300 K with low coercivity $H_C = 0.9$ mT and a very high magnetization M_s close to 70 $Am^2\ kg^{-1}$. This magnetization value is among the highest values reported in the literature but obtained by using various preparation techniques requiring heating and/or annealing treatment. The radiation-induced reduction method under normal temperature and pressure conditions has proven to be extremely efficient to synthesize ultra-small superparamagnetic nanoparticles of cobalt ferrite. The magnetic properties of these NPs can be exploited for MHT processes.

Conflicts of interest

There are no conflicts to declare.

Acknowledgements

The authors acknowledge Antoine Raison and François Brisset from ICMMO for their help in XRD measurements and HRTEM analysis.

References

1 R. Hudson, Y. Feng, R. S. Varma and A. Moores, *Green Chem.*, 2014, **16**, 4493–4505.

2 E. Raymenants, O. Bultynck, D. Wan, T. Devolder, K. Garello, L. Souriau, A. Thiam, D. Tsvetanova, Y. Canvel and D. Nikonov, *Nat. Electron.*, 2021, **4**, 392–398.

3 G. Reiss and A. Hütten, *Nat. Mater.*, 2005, **4**, 725–726.

4 B. Dieny, I. L. Prejbeanu, K. Garello, P. Gambardella, P. Freitas, R. Lehndorff, W. Raberg, U. Ebels, S. O. Demokritov and J. Akerman, *Nat. Electron.*, 2020, **3**, 446–459.

5 M. M. Yallapu, S. F. Othman, E. T. Curtis, B. K. Gupta, M. Jaggi and S. C. Chauhan, *Biomaterials*, 2011, **32**, 1890–1905.

6 R. A. Frimpong and J. Z. Hilt, *Nanomedicine*, 2010, **5**, 1401–1414.

7 I. J. Bruvera, P. Mendoza Zélis, M. Pilar Calatayud, G. F. Goya and F. H. Sánchez, *J. Appl. Phys.*, 2015, **118**, 184304.

8 H. Gavilán, S. K. Avugadda, T. Fernández-Cabada, N. Soni, M. Cassani, B. T. Mai, R. Chantrell and T. Pellegrino, *Chem. Soc. Rev.*, 2021, **50**, 11614–11667.

9 H. M. Joshi, Y. P. Lin, M. Aslam, P. Prasad, E. A. Schultz-Sikma, R. Edelman, T. Meade and V. P. Dravid, *J. Phys. Chem. C*, 2009, **113**, 17761–17767.

10 G. Wang, F. Zhou, X. Li, J. Li, Y. Ma, J. Mu, Z. Zhang, H. Che and X. Zhang, *Ceram. Int.*, 2018, **44**, 13588–13594.

11 J. Pan, P. Hu, Y. Guo, J. Hao, D. Ni, Y. Xu, Q. Bao, H. Yao, C. Wei and Q. Wu, *ACS Nano*, 2020, **14**, 1033–1044.

12 W. M. O. De Santana, S. Abramson, R. Fini, B. L. Caetano, C. Ménager, S. H. Pulcinelli and C. V. Santilli, *ACS Appl. Polym. Mater.*, 2021, **3**, 4837–4848.

13 S. G. Mendo, A. F. Alves, L. P. Ferreira, M. M. Cruz, M. H. Mendonça, M. Godinho and M. D. Carvalho, *New J. Chem.*, 2015, **39**, 7182–7193.

14 J. Thomas, N. Thomas, F. Girgsdies, M. Beherns, X. Huang, V. Sudheesh and V. Sebastian, *New J. Chem.*, 2017, **41**, 7356–7363.

15 S. F. Shams, M. Kashefi and C. Schmitz-Antoniak, *New J. Chem.*, 2018, **42**, 3050–3062.

16 A. V. Raut, D. Kurmude, D. Shengule and K. Jadhav, *Mater. Res. Bull.*, 2015, **63**, 123–128.

17 M. Sanna Angotzi, A. Musinu, V. Mameli, A. Ardu, C. Cara, D. Niznansky, H. L. Xin and C. Cannas, *ACS Nano*, 2017, **11**, 7889–7900.

18 P. Palade, C. Comanescu, A. Kuncser, D. Berger, C. Matei, N. Iacob and V. Kuncser, *Nanomaterials*, 2020, **10**, 476.

19 H. Zhang, L. Liu and X. Liu, *ACS Nano*, 2017, **11**, 3614–3631.

20 R. A. Bohara, N. D. Thorat, H. M. Yadav and S. H. Pawar, *New J. Chem.*, 2014, **38**, 2979–2986.

21 T. Gaudisson, M. Artus, U. Acevedo, F. Herbst, S. Nowak, R. Valenzuela and S. Ammar, *J. Magn. Magn. Mater.*, 2014, **370**, 87–95.

22 K. E. Mooney, J. A. Nelson and M. J. Wagner, *Chem. Mater.*, 2004, **16**, 3155–3161.

23 J. Marignier, J. Belloni, M. Delcourt and J. Chevalier, *Nature*, 1985, **317**, 344–345.

24 J. Belloni and M. Mostafavi, *Studies in Physical and Theoretical Chemistry*, Elsevier, 2001, vol. 87, pp. 411–452.

25 J. Belloni, J.-L. Marignier and M. Mostafavi, *Radiat. Phys. Chem.*, 2020, **169**, 107952.

26 A. Souici, N. Keghouche, J. Delaire, H. Remita, A. Etcheberry and M. Mostafavi, *J. Phys. Chem. C*, 2009, **113**, 8050–8057.

27 A. Souici, K.-L. Wong, V. De Waele, J. Marignier, T. H. Metzger, N. Keghouche, S. Mintova and M. Mostafavi, *J. Phys. Chem. C*, 2014, **118**, 6324–6334.

28 J. Belloni, M. Mostafavi, H. Remita, J.-L. Marignier and M.-O. Delcourt, *New J. Chem.*, 1998, **22**, 1239–1255.

29 P. Mulvaney and A. Henglein, *J. Phys. Chem.*, 1990, **94**, 4182–4188.

30 I. Marić, G. Dražić, G. Štefanić, K. Zadro, M. Gotić and T. Jurkin, *Mater. Charact.*, 2020, **159**, 110038.

31 T. Jurkin, M. Gotić, G. Štefanić and I. Pucić, *Radiat. Phys. Chem.*, 2016, **124**, 75–83.

32 S. Wang and H. Xin, *Radiat. Phys. Chem.*, 1999, **56**, 567–572.

33 Z. Li, Y. Yang, A. Relefors, X. Kong, G. M. Siso, B. Wickman, Y. Kiros and I. L. Soroka, *J. Colloid Interface Sci.*, 2021, **583**, 71–79.

34 P. Mulvaney, L. Denison, F. Grieser, R. Cooper, J. V. Sanders and D. Meisel, *J. Colloid Interface Sci.*, 1988, **121**, 70–80.

35 L. Alrehaily, J. Joseph, M. Biesinger, D. Guzonas and J. Wren, *Phys. Chem. Chem. Phys.*, 2013, **15**, 1014–1024.

36 S.-W. Kim, B.-J. Kwon, J.-H. Park, M.-G. Hur, S.-D. Yang and H. Jung, *Bull. Korean Chem. Soc.*, 2010, **31**, 910–914.

37 S.-H. Choi, Y.-P. Zhang, A. Gopalan, K.-P. Lee and H.-D. Kang, *Colloids Surf., A*, 2005, **256**, 165–170.

38 M. Kurakula and G. K. Rao, *Drug Delivery Sci. Technol.*, 2020, **60**, 102046.

39 G. V. Buxton, C. L. Greenstock, W. P. Helman and A. B. Ross, *J. Phys. Chem. Ref. Data*, 1988, **17**, 513–886.

40 L. Lutterotti, *Nucl. Instrum. Methods Phys. Res., Sect. B*, 2010, **268**, 334–340.

41 I. Marić, M. Gotić, G. Štefanić, A. Pustak and T. Jurkin, *Radiat. Phys. Chem.*, 2020, **170**, 108648.

42 D. Gallant, M. Pezolet and S. Simard, *J. Phys. Chem. B*, 2006, **110**, 6871–6880.

43 W. Wei, W. Chen and D. G. Ivey, *Chem. Mater.*, 2008, **20**, 1941–1947.

44 N. McIntyre and D. Zetaruk, *Anal. Chem.*, 1977, **49**, 1521–1529.

45 T. Yamashita and P. Hayes, *Appl. Surf. Sci.*, 2008, **254**, 2441–2449.

46 H. Liu, G. Wei, Z. Xu, P. Liu and Y. Li, *Appl. Surf. Sci.*, 2016, **389**, 438–446.

47 A. Grosvenor, B. Kobe, M. Biesinger and N. McIntyre, *Surf. Interface Anal.*, 2004, **36**, 1564–1574.

48 R. D. Diehl and R. McGrath, *Surf. Sci. Rep.*, 1996, **23**, 43–171.

49 P. M. Kouotou, H. Vieker, Z. Tian, P. T. Ngamou, A. El Kasmi, A. Beyer, A. Gölzhäuser and K. Kohse-Höinghaus, *Catal. Sci. Technol.*, 2014, **4**, 3359–3367.

50 G. Allen and K. Hallam, *Appl. Surf. Sci.*, 1996, **93**, 25–30.

51 G. Barrera, P. Tiberto, P. Allia, B. Bonelli, S. Esposito, A. Marocco, M. Pansini and Y. Leterrier, *Appl. Sci.*, 2019, **9**, 212.

52 B. Cai, M. Zhao, Y. Ma, Z. Ye and J. Huang, *ACS Appl. Mater. Interfaces*, 2015, **7**, 1327–1333.

53 D. Li, H. Yun, B. T. Diroll, V. V. Doan-Nguyen, J. M. Kikkawa and C. B. Murray, *Chem. Mater.*, 2016, **28**, 480–489.

54 S. Chandra, H. Khurshid, W. Li, G. Hadjipanayis, M. Phan and H. Srikanth, *Phys. Rev. B: Condens. Matter Mater. Phys.*, 2012, **86**, 014426.

55 S. M. Ansari, B. B. Sinha, D. Phase, D. Sen, P. U. Sastry, Y. D. Kolekar and C. V. Ramana, *ACS Appl. Nano Mater.*, 2019, **2**, 1828–1843.

56 C. Tannous and J. Gieraltowski, *Eur. J. Phys.*, 2008, **29**, 475.

57 K. L. Routray, D. Sanyal and D. Behera, *Mater. Res. Bull.*, 2019, **110**, 126–134.

58 T. Hyeon, Y. Chung, J. Park, S. S. Lee, Y.-W. Kim and B. H. Park, *J. Phys. Chem. B*, 2002, **106**, 6831–6833.

59 A. Raut, D. Kurmude, S. Jadhav, D. Shengule and K. Jadhav, *J. Alloys Compd.*, 2016, **676**, 326–336.

60 N. Moumen and M. Pileni, *J. Phys. Chem.*, 1996, **100**, 1867–1873.

61 M. S. Darwish, H. Kim, H. Lee, C. Ryu, J. Y. Lee and J. Yoon, *Nanomaterials*, 2019, **9**, 1176.

62 P. Kumar, S. Pathak, A. Singh, H. Khanduri, G. Basheed, L. Wang and R. Pant, *Nanoscale Adv.*, 2020, **2**, 1939–1948.

63 A. P. Herrera, L. Polo-Corrales, E. Chavez, J. Cabarcas-Bolivar, O. N. Uwakweh and C. Rinaldi, *J. Magn. Magn. Mater.*, 2013, **328**, 41–52.